

<https://doi.org/10.1038/s43247-024-01244-7>

# Blind magmatism abets nonvolcanic continental rifting

Check for updates

Rasheed Ajala<sup>1</sup> ✉, Folarin Kolawole<sup>1</sup> & William Menke<sup>1</sup>

Tectonic forces alone cannot drive rifting in old and thick continental lithosphere. Geodynamic models suggest that thermal weakening is critical for lithospheric extension, yet many active rifts lack volcanism, seeming to preclude this process. We focus on one such rift, the Tanganyika-Rukwa segment of the East African Rift System, where we analyze local seismicity for shear wave anisotropy and couple the results with numerical modeling. The strongest splitting measurements are from earthquakes with paths sampling lower crustal regions of high compressional-to-shear wave velocity ratios and have fast polarization directions parallel to the local mantle flow, implying the existence of oriented melt lenses. This lower crustal magmatism and observed high surface heat flow are consistent with substantial lithospheric weakening and explain the enigmatic relief and increasing strain accommodation along the rift axis. We conclude that progressive nonvolcanic rifting is assisted by deep crustal melts yet to breach the surface.

In the Wilson Cycle, divergent plate boundaries are initiated by the rifting of continental lithosphere, leading to continental break up and the creation of oceanic crust along oceanic spreading centers<sup>1</sup>. Several competing geological and geodynamic factors control the breakup mechanism and determine rift configuration throughout the extension lifecycle<sup>2</sup>. However, a long-standing question remains on the rifting of the thick, old, cold continental lithosphere—a problem encapsulated by the tectonic force paradox<sup>3</sup>. The cratonic lithospheric strength far exceeds the available tectonic forces, implying that rifting requires other major driving mechanisms for weakening. Resolving this paradox will provide insight into the breakup of past supercontinents. Geodynamic models commonly employ thermal anomalies to promote strain localization by eroding the lithospheric mantle<sup>2</sup>. However, several active nonvolcanic (amagmatic, magma-poor) rifts with extensive crustal deformation show only minor lithospheric thinning<sup>4</sup>. Similarly, rifted margins show segments of voluminous volcanism and pervasive magmatic intrusions<sup>5</sup> as well as segments with little or no volcanism<sup>6</sup>. Although inherited crustal and lithospheric structures may help to nucleate rift faulting, their influence on continued strain accommodation may not persist beyond the early stages of tectonic extension<sup>2</sup>. Thus, an important knowledge gap remains on how persistent tectonic strain is being accommodated along active continental rift zones where there is no evidence of volcanism.

The Cenozoic East African Rift System (EARS; Fig. 1a) is the largest active continental rift system on Earth. It is associated with the eastward deflection of rising hot materials from a mantle plume source that results in a

magma-rich eastern branch and a magma-starved western branch<sup>7</sup>. Although magma-poor, the western branch has a few localized volcanic centers, among which are the Rungwe Volcanic Province just north of the Malawi Rift and the Virunga Volcanic Province in the Kivu Rift located further north (Fig. 1a). In between these volcanic areas is the broad non-volcanic section of the rift branch hosting the NW-trending Tanganyika-Rukwa Rift Zone (Fig. 1b). Regional tomographic models show shear wave velocities indicative of unelevated mantle temperatures<sup>8</sup>. The rift zone is characterized by broad and elevated rift flanks, long border faults, and basins with tectonic extension that accommodate >7 km deep sedimentary basins of Mesozoic–Cenozoic age<sup>9</sup>. The rifts are surrounded by the Bangweulu and Tanzania cratons, with estimated lithospheric thicknesses up to 200 km<sup>4</sup>, and Proterozoic mobile belts with northwest-trending regional strain fabrics, which the rifts exploit during their development<sup>10</sup>. Seismic activity in the area is high, having hosted one of the largest African earthquakes in recent history, the 1910  $M_w$  7 Rukwa Rift earthquake event<sup>11</sup>. Within the southern Tanganyika Rift, earthquakes extend down to the lower crust and upper mantle (Fig. 1b, c). The rift hosts a narrow zone of increasing axial strain<sup>12</sup> manifested by the collocation of clustered intra-rift faults featuring a prominent fault-bounded syn-rift wedge that increases in thickness with time (S1 to S3–6), at the deepest parts of the lake bed (e.g., white arrow in B–B' in Fig. 1b inset).

The timing of Cenozoic rift initiation is not well-determined. Uranium-lead dating of carbonatitic tuffs in the Rungwe Volcanic Province suggests an upper bound of 25 Ma<sup>13</sup>, and detrital zircon dating of the Rukwa

<sup>1</sup>Lamont-Doherty Earth Observatory, Columbia University, Palisades, NY, USA.✉ e-mail: [rajala@ldeo.columbia.edu](mailto:rajala@ldeo.columbia.edu)

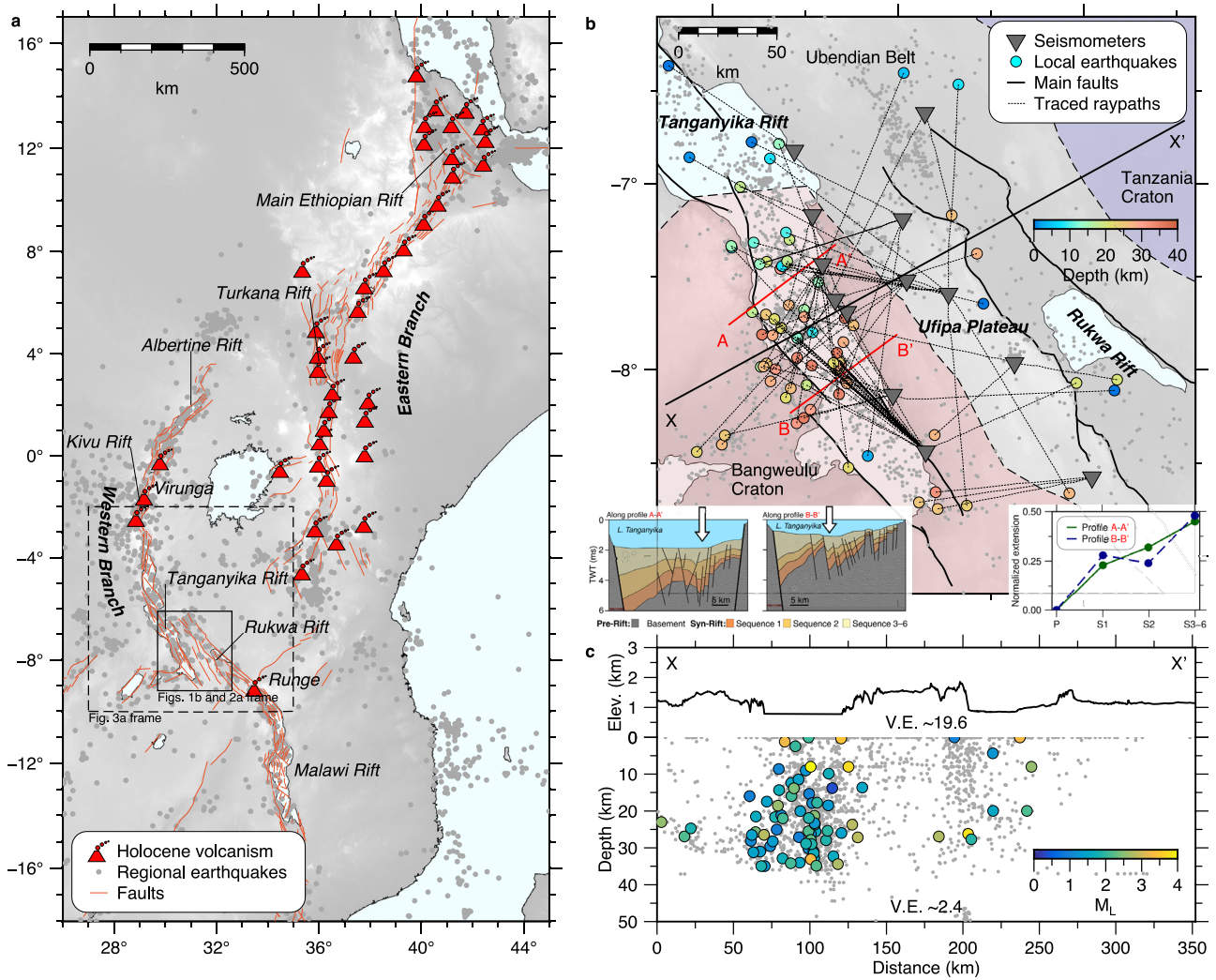


**Fig. 1 | Study area maps of the East African Rift System.** **a** Rift faults, earthquakes, and volcanic centers highlight the dichotomy of the western and eastern rift branches. **b** Tanganyika-Rukwa Rift Zone showing the locations of the seismometers and earthquakes used in the analysis<sup>20</sup>. Colored polygons define Archean cratons and Proterozoic mobile belts. *Bottom left inset*: seismic reflection profiles with

interpretations<sup>12</sup>, showing that although both the border fault and rift axis are accommodating considerable tectonic strain, extension at the rift axis is increasing (*bottom right inset*). **c** Seismicity depth profile. Color-coded earthquakes in panels **b** and **c** represent events with reliable shear wave splitting measurements.

Lake sediments gives a lower bound of 8 Ma<sup>14</sup>. Geochemical analysis of nearby volcanic rocks indicates a plume source<sup>15</sup>. Until recently, geophysical monitoring has been too sparse to provide a detailed view of subsurface processes in the Tanganyika-Rukwa Rift Zone. The deployment of broadband seismographs has allowed some constraints on the crustal structure, which reveals that the crust has accommodated up to 20% extension and has anomalously high compressional-shear wave velocity ratios comparable to the magma-rich Main Ethiopian Rift in the eastern branch<sup>16,17</sup>. Observations of mantle anisotropy indicate a dominant rift-parallel (NW-trending) orientation, interpreted to be associated with a local deflection of the regional mantle flow by the surrounding cratons and oriented melt pockets in the upper mantle<sup>18</sup>. Combined with observations of high surface heat flow and hydrothermal activities<sup>19</sup>, these previous results hint at a subsurface magmatic influence.

We present crustal seismic anisotropy of the Tanganyika-Rukwa Rift Zone using a seismic waveform database and associated local earthquake catalog<sup>20</sup> developed from the TANGA14 seismic array, which was deployed on the Ufipa Plateau between the Tanganyika and Rukwa Rift basins (Fig. 1b). Shear wave splitting analysis reveals fast polarization orientations of the shear waves and the corresponding strength of the anisotropy normalized over the entire ray path of the associated earthquake (Fig. 2). The

strongest anisotropy is measured along ray paths that sample the middle-to-lower crust and are collocated with areas having high compressional-shear wave velocity ratios; thus, confirming the presence of oriented melt pockets, including volatiles, in the crust. These results and surface heat flow measurements explain the enigmatic topography (Fig. 3) of the rift flanks and indicate that lower crustal magmatism with no surface manifestation is responsible for the reduction in lithospheric strength that is driving rifting (Fig. 4).

## Results and discussion

### Coupled mantle and crustal anisotropy

Seismic anisotropy is the directional dependence of seismic wave velocity polarization that provides information about rock fabric<sup>21</sup>. The most dominant form of anisotropy in the mantle, Lattice Preferred Orientation (LPO), is caused by the strain-induced alignment of olivine crystals<sup>22</sup>. In the crust, anisotropy is commonly attributed to Shape Preferred Orientation (SPO)<sup>23</sup> caused by lithologic layering or oriented inclusions, such as water-filled fractures or aligned melt lenses. Analysis of SPO in the crust and LPO in the mantle can be used to explore deep crustal processes in the Tanganyika-Rukwa Rift Zone that subsurface imaging techniques cannot resolve due to the poor spatial density of existing geophysical datasets. These

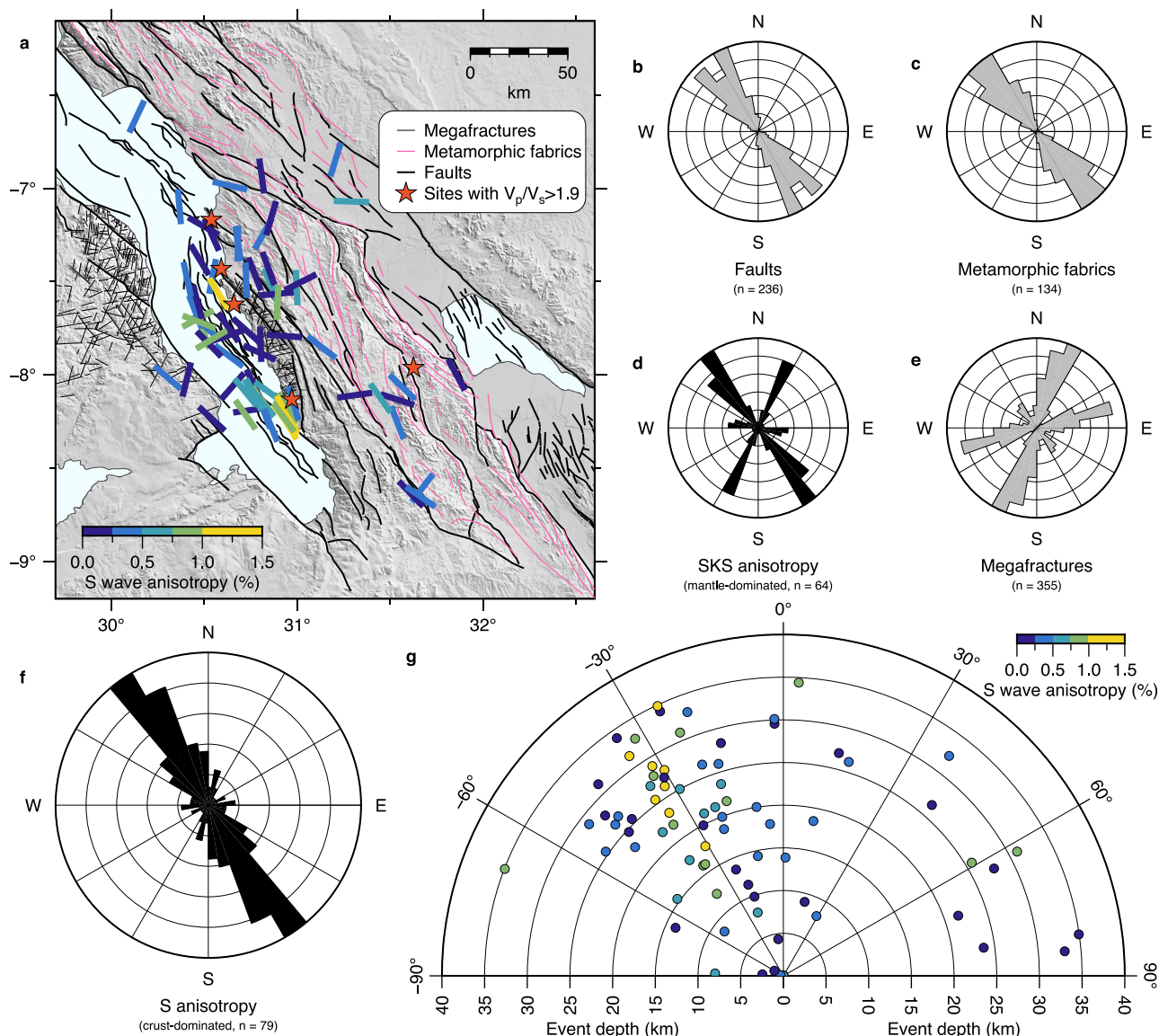


**Fig. 2 | Crustal seismic anisotropy results compared with previous mantle anisotropy and surficial trends.** **a** Map of shear wave splitting results plotted at the midpoint of their ray paths and colored using the shear wave anisotropy. **b–f** Rose orientation plots for the rift faults, pre-rift Precambrian metamorphic fabrics,

mantle anisotropy<sup>18</sup>, megafractures, and crustal anisotropy. **g** Polar plot showing the anisotropy results as a function of the earthquake depth and northern direction of the polarization orientations and colored using the shear wave anisotropy.

include the existing receiver function database, which provides estimates of the bulk compressional-shear velocity ratios and crustal thicknesses in the Ubendian Belt<sup>16</sup> but whose poor depth resolution precludes discriminating possible mechanisms for variations in these properties.

We determine seismic anisotropy in the crust using shear wave splitting measurements from local earthquakes recorded by 13 broadband three-component seismometers deployed from June 2014 to September 2015<sup>16</sup>. High-quality measurements are made using earthquakes with 0–35 km depths, a range that is entirely within the crust<sup>16</sup>. The splitting measurements show patterns of dominant rift-parallel northwest fast polarization axes that are subparallel to the active faults and pre-rift basement metamorphic shear zones (Fig. 2b, c, f). Less prevalent trends have subparallel orientations to the megafractures mapped on granitic terranes within the Bangweulu Craton (Fig. 2e). The strength of anisotropy is largest for events occurring in the lower crust (Fig. 2g) and propagation paths that sample the region beneath the southern Tanganyika Rift with high compressional-shear wave velocity ratios (Figs. 1b and 2a). Shallower events that sample this same region have weaker seismic anisotropy (Fig. 2a). As the strength of anisotropy dramatically increases with hypocentral depth, we hypothesize that the anisotropy

is associated with SPO caused by melt pocket alignment, restricted to the lower crust, and is also the source of the high compressional-shear wave velocity ratios beneath the seismic stations. The weaker anisotropy from shallower events may be due to basement metamorphic fabrics or fluid-filled fractures.

Shear wave splitting from teleseismic SKS waves<sup>18</sup>, which sample the whole lithosphere and asthenosphere, has two dominant fast-axis orientations: northwest and northeast (Fig. 2d). The northwest trend is interpreted to result from mantle flow that deflected around the Bangweulu Craton into the Tanganyika-Rukwa Rift Zone, inducing vertical flow that generates oriented melt pockets in the upper mantle<sup>18</sup>. The northeast trend is attributed to LPO from the regional plate motion<sup>18</sup>. The similarity of the orientation of the crustal and SKS fast axes (both about N30°W) indicates that melt-induced anisotropy extends from the upper mantle into the lower crust and provides strong evidence for melt emplacement in the lower crust and upper mantle beneath the rift axis. These crustal anisotropy observations can be explained by vertically aligned and horizontally oriented melt channels in the lower crust along the rift axis<sup>24</sup>.

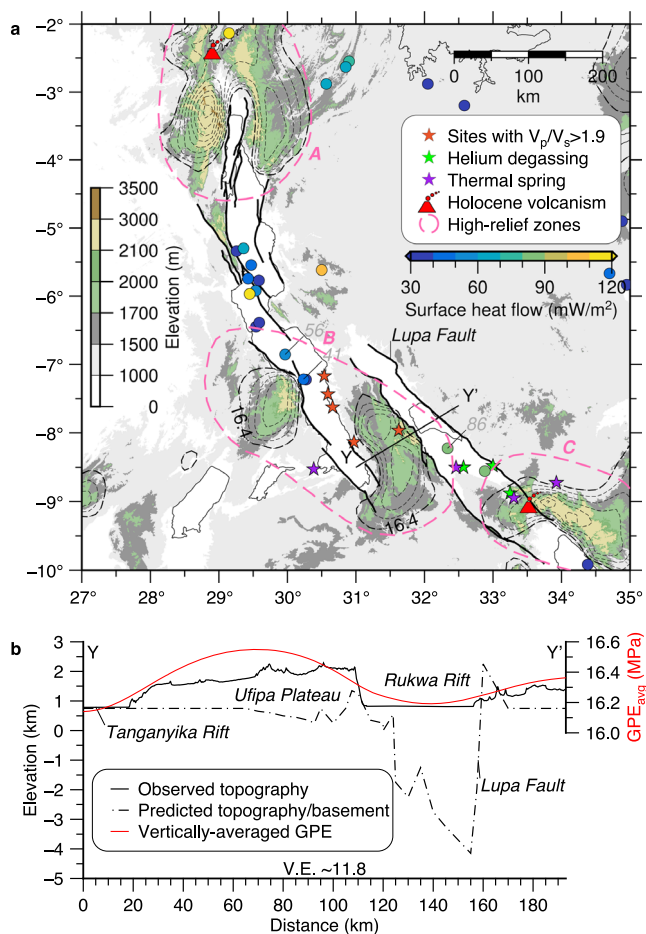


**Fig. 3 | Topographic anomalies.** **a** Polygons labeled A, B, C highlight the three high-relief zones in the region. Other symbols indicate a compilation of surface heat flow measurements, sites with high compressional-shear wave velocity ratios, helium degassing, thermal springs, and volcanism. The black line indicates the profile below in **(b)**. **b** Results of a flexural cantilever model<sup>9</sup> compared with topography and the vertically averaged gravitational potential energy (GPE)<sup>50</sup>.

Above the zone of strong crustal anisotropy in the southern Tanganyika Rift, tectonic extension is accommodated by both the border and intra-rift faults<sup>12</sup>, and increasingly on the intra-rift faults (S3–6 in Fig. 1b insets). This pattern of rift faulting is anomalous for early-stage magma-poor rifts since strain localizes at the rift axis during the later phases of extension<sup>25–27</sup>. While unusual, rifting in the region may have evolved beyond the earliest phases, such that the rift axis is approaching the onset of strain localization. Inherited orogenic shear zones commonly focus on early intra-rift faulting<sup>28</sup>; however, this is unlikely the case in the southern Tanganyika Rift as the rift is not within a mobile belt (Fig. 1b).

### Thermally supported surface elevations

Although surface magmatism in the region is absent, other geological observations suggest the existence of deep thermal anomalies, including high surface heat flow, hydrothermal vents, and helium-degassing zones<sup>19,29</sup>. A major unexplained feature of the rift zone is its anomalously high topographic relief (high-relief zone ‘B’ in Fig. 3a). Similar high and broad regions of elevated topography occur north of the Tanganyika Rift (high-relief zone ‘A’) and south of the Rukwa Rift (high-relief zone ‘C’), which are associated with surface volcanism (Fig. 3a). The ~400 km wavelength of these features is too large to be associated with footwall uplift from normal faulting but may be too small to be a result of dynamic topography due to a regionally impinging mantle plume<sup>30</sup>. Flexural

cantilever models fail to produce the elevation or wavelength of the observed topography (Fig. 3b) with elevation underprediction exceeding 1.5 km<sup>9</sup> even when using grossly underestimated elastic thickness values<sup>31</sup>; altogether, indicating the influence of an external and relatively local control.

We explain these topographic anomalies by considering the isostatic effects of lower crustal melting, including volatiles, and elevated mantle temperatures<sup>32</sup>. The complex evolution of the rift zone, imprecise timing of rift initiation, and the absence of erupted volcanic materials for geochemical analysis to lend insight into the melt source preclude a sophisticated thermo-mechanical model. Therefore, we approximate the geothermal evolution model in the Tanganyika-Rukwa Rift zone (zone B in Fig. 3) using a set of steady-state geotherms corresponding to the approximate range of observed surface heat flow measurements (Fig. 4b), where the smallest and largest values correspond to the craton and most mature part of the rift zone respectively and do not consider any specific rheology as it remains mostly unknown. The depth of the 1300 °C isotherm, which is a proxy for the lithosphere-asthenosphere boundary, is generally consistent with regional values from previous studies<sup>4,33,34</sup>; a constant 40 km crustal thickness is assumed, close to the observed average. These geotherms are used to model the evolution of the lithospheric yield strength envelope (Fig. 4c) and the topographic uplift (Fig. 4a).

The maximum plausible melt and volatile fraction in the lower crust is 0.2, estimated using liquidus and solidus relations<sup>35</sup> for common lower crustal mafic rocks like gabbro and the highest observed surface heat flow value of ~90 mW m<sup>-2</sup> (Zone B in Fig. 3a). Were the bottom 20 km of the crust to have this melt fraction, isostasy would cause approximately 400 m of uplift. Thermal isostatic effects from lithospheric mantle thinning can account for the remaining 1100 m of the observed relief (Fig. 4a), even accounting for variable erosion<sup>12</sup>. These results suggest a decoupling in the amount of deformation in the area since the extension in the crust is considerably less than what is predicted in the mantle by the geotherms. Without explicit consideration of magmatism on the lithospheric strength envelope, the evolution in the strength profile following the geotherms shows a substantial decrease in the lithospheric strength to values within the range of tectonic forces (1–5 TN m<sup>-1</sup>).

### Implications for amagmatic continental rifting

Our model has deep crustal melts and volatiles resulting from thermal perturbations from the mantle, promoting crustal weakening and tectonic deformation in the absence of surface volcanism. In our study, measurements of crustal anisotropy from seismic data show a strong dependence on lower crustal melt distribution, representing ‘blind melts’ that are yet to breach the surface, possibly due to the low permeability of existing deep fault networks<sup>30</sup> (Fig. 4d). Along the western branch, previous geophysical surveys have lacked the spatial resolution to detect low-volume melts that are trapped within the deep crystalline crust and upper-mantle, leading to the supposition that they were not present<sup>8</sup>. However, recent geophysical models developed using sophisticated imaging algorithms show that the upper mantle beneath the western branch may not be as cold as previously suggested, with low shear wave velocity anomalies beneath the study area<sup>36</sup>. Our findings present compelling evidence that links lower crustal magmatism with its influence on thermal isostasy, lithospheric weakening, and strain accommodation in nonvolcanic rift settings. We argue that during nonvolcanic rifting, the persistence of tectonic extension and initiation of strain localization at the rift axis is assisted by deep crustal melts and volatiles (Fig. 4d).

Studies of the volcanic phases of large igneous provinces show that an enormous amount of degassing can occur thousands of years before the arrival of the magma at the surface<sup>37</sup>. Consequently, deep ‘blind melts’ in nonvolcanic active continental rifts have implications for climate change because they might act as a source of diffuse and yet undetected volatiles, e.g., carbon dioxide emissions. Overall, the findings in this study highlight that a better understanding of blind melting products beneath nonvolcanic rifts requires higher-resolution geophysical detection analyses<sup>38</sup>.

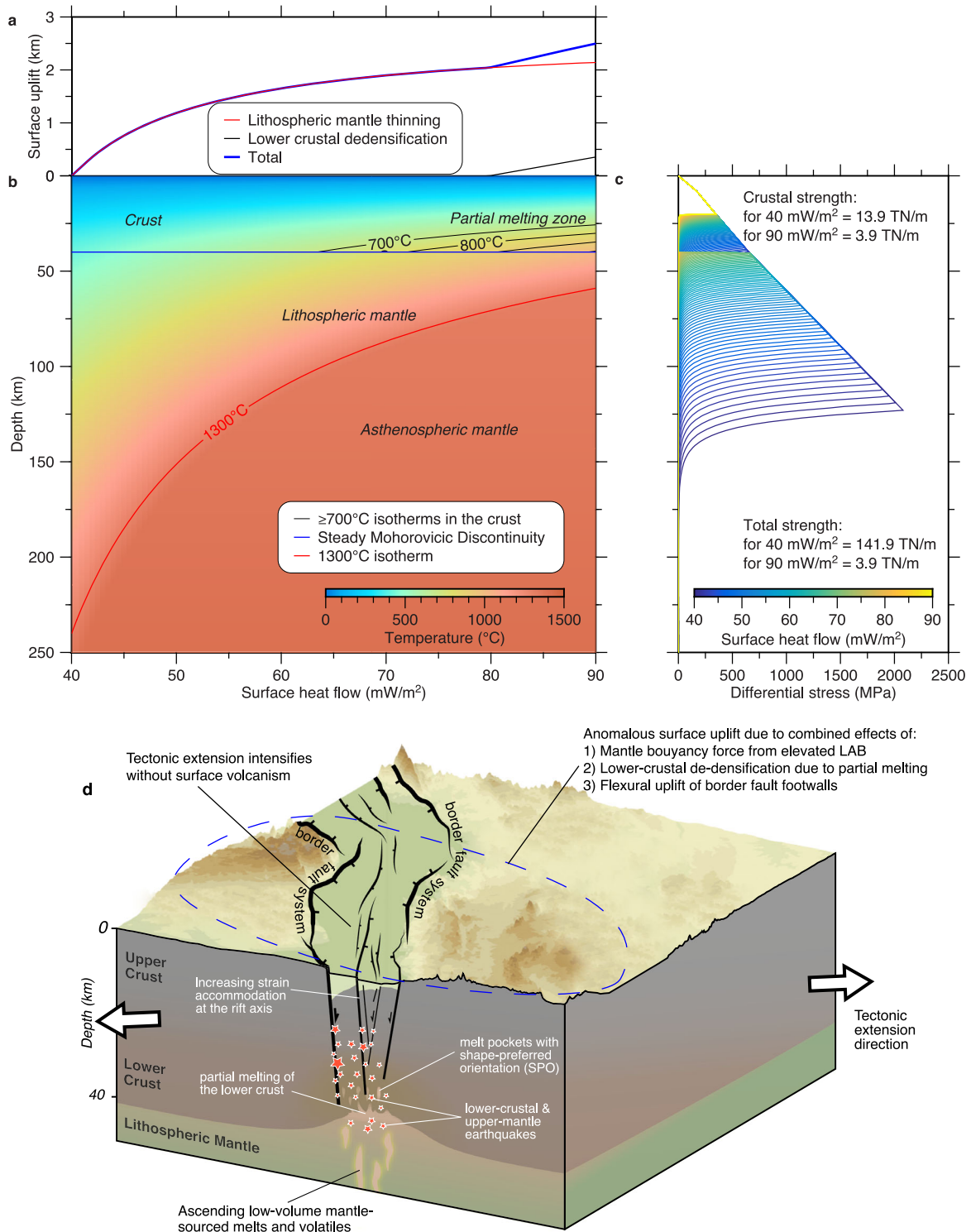


**Fig. 4 | One-dimensional (1D) thermo-rheological model showing the isostatic contribution to the surface elevation and decreasing lithospheric strength due to evolving surface heat flow. a** Predicted surface uplift from a combination of lower crustal dedensification and lithospheric mantle thinning. **b** Geothermal evolution

based on the observed range of surface heat flow measurements. **c** Yield strength envelope corresponding to geotherms in (b). **d** Schematic summary of the proposed mechanism driving continued extension and transition to rift-axial strain localization along nonvolcanic active rifts.

## Methods

### Crustal seismic anisotropy

We use the minimum-eigenvalue shear wave splitting technique with cluster analysis as implemented in the MFAST<sup>39</sup> program to obtain the seismic anisotropy measurements. The method does not require knowledge of the initial polarization of the shear waves. A numerical grid search over a range

of polarization orientations and delay times is used to determine the optimal parameters that linearize the particle motions on the horizontal components and unsplit the shear waves within a selected seismogram window. All shear wave splitting results are manually inspected to ensure that they meet high-quality selection criteria, including a minimum signal-to-noise ratio of 3, maximum delay time between the fast and slow shear wave of 0.3 s, and

uncertainties in delay times and polarization orientations of less than 0.03 and 16°, respectively. Null split measurements with initial polarization orientations within 20° of the fast polarization orientations are discarded. Supplementary Fig. 1 shows an example of a high-quality shear wave splitting result. The complete list of the most reliable shear wave splitting results is listed in the Supplementary Data.

### Data

We use the continuous seismic data from the TANGA14 array comprising 13 broadband seismometers and deployed for a 15-month period from June 2014 to September 2015. The anisotropy analysis was performed using the recently developed local earthquake catalog consisting of 2213 earthquakes<sup>20</sup>. S phase picking was performed manually on filtered traces, resulting in a total of 3121 picks from 1261 events. Roughly 3% (79) of the S picks led to reliable shear wave splitting measurements.

### Ray tracing

To compute the S wave anisotropy (SWA) and obtain better estimates of the incident angles for further refinement of the shear wave splitting results, we compute raypaths in a 3D volume using a radially symmetric velocity model<sup>20</sup> rather than using a straight-line approximation that would be suitable for a homogenous media. For each source, we compute the travel time field by solving the eikonal equation<sup>40</sup>:

$$\|\nabla t(\mathbf{x})\|_2 = s(\mathbf{x})^2, \quad (1)$$

where  $t(\mathbf{x})$  is the space-dependent  $\mathbf{x}$  travel time field,  $\|\cdot\|_2$  is the Euclidean norm, and  $s(\mathbf{x})$  is slowness defined as the inverse of velocity. For computational efficiency, we treat the seismometers as sources and compute only 13 travel time fields. We then simultaneously trace the raypaths between each receiver and any number of events using the gradient of the travel time field (Supplementary Fig. 2). The calculated incident angle is also corrected for topographic slope, which is nearly zero at most stations. We take caution to avoid the misinterpretation of the effect of S-to-P headwave conversions at the free surface as shear wave splitting by ensuring that the incident angle of the rays fall within the shear wave window at each station given as  $\sin^{-1}\left(\frac{v_s}{v_p}\right)$ , where  $v_s$  and  $v_p$ , are the shear and compressional wave velocity at the receiver location<sup>41</sup>.

### Anisotropic strength

We compute the S wave anisotropy (SWA), which normalizes the observed delay times  $\delta t$  using the average shear wave velocities  $v$  and distance  $d$  along each raypath, to better localize the source of the strongest anisotropic signal:

$$SWA = \left( \sqrt{4 + \left(\frac{2d}{v\delta t}\right)^2} - \frac{2d}{v\delta t} \right) \times 100. \quad (2)$$

We focus on interpreting the S wave anisotropy (SWA) rather than the delay time between the polarized fast and slow shear waves due to the dependence of the latter on the ray path distance, which can lead to ambiguity in interpretation (Supplementary Figs. 3 and 4). SWA measures the fractional perturbation of the average S wave velocity along the ray path, which normalizes the effect of distance and the sampled velocity structure<sup>42</sup>. However, we note that the absolute value of SWA in Fig. 2 is not as important as the relative value since anisotropy is assumed to be accrued along the entire ray path. Thus, SWA values may be higher when normalized only over the shorter ray path segments within the true anisotropic domain or when straight-line ray paths are assumed.

### Geothermal evolution

We use the range of surface heat flow measurements in the area (zone B in Fig. 3a) to compute lower-bound geotherms that may represent the geothermal evolution. Thus, the evolution is realized as a set of steady-state

geotherms by solving the Poisson form of the temperature equation<sup>43</sup>:

$$\nabla^2 T = -\frac{H}{k}, \quad (3)$$

where  $T$  (°C) is the temperature field,  $H$  ( $\mu\text{W m}^{-3}$ ) is the volumetric heat production, and  $k$  is the thermal conductivity. Using both the surface heat flow  $q_0$  ( $\text{mW m}^{-3}$ ) and surface temperature  $T_0$  as boundary conditions and integrating Eq. 3 twice yields:

$$q_0 = q_z + Hz, \quad (4)$$

and

$$T_z = T_0 + \frac{q_0}{k}z - \frac{H}{2k}z^2, \quad (5)$$

where  $k$  ( $\text{W m}^{-1} \text{K}^{-1}$ ) is the thermal conductivity.

The surface heat flow in the upper crust is partitioned to be 40% from radiogenic sources and 60% from deeper mantle sources, with an exponentially decreasing volumetric heat production:

$$H(z) = H_0 \exp\left(-\frac{z}{D}\right), \quad (6)$$

$$H_0 = 0.4 \times \frac{q_0}{D}, \quad (7)$$

where  $D$  is the radiogenic length taken to be 10 km, consistent with empirical studies around the world<sup>44</sup> and  $H_0$  is the surface radiogenic heat production. We allow the upper crustal volumetric heat production to decay until it matches the value in the lower crust or crosses the Conrad discontinuity. The convective geotherm in the asthenosphere is computed using a potential mantle temperature of 1300 °C and an adiabatic gradient of 0.4 K km<sup>-1</sup>.

### Yield strength envelope

For each geotherm, we compute the associated yield strength envelope using brittle and ductile flow laws. The thickness of the upper and lower crust is kept constant at 20 km but the thicknesses of the lithospheric and asthenospheric mantle is allowed to vary depending on the lithosphere-asthenosphere boundary determined using the 1300 °C isotherm in the geotherms. For the brittle layer, we compute the differential stress  $\sigma$  as

$$\sigma = \begin{cases} 0.85 \times P, & P < 0.2 \text{ GPa} \\ 0.5 + 0.6 \times P, & \text{Otherwise} \end{cases}, \quad (8)$$

where  $P$  is the lithostatic pressure. The diffusion creep follows the power law:

$$\dot{\epsilon} = A\sigma^n d^{-m} f_{H_2O}^r \exp\left(-\frac{Q + PV}{RT}\right), \quad (9)$$

where  $\dot{\epsilon}$  is the strain rate ( $1e-15 \text{ s}^{-1}$ )<sup>45</sup>,  $A$  is the pre-exponential material constant,  $n$  is the differential stress exponent equaling 1 for diffusion creep,  $f_{H_2O}$  is the water fugacity with exponent  $r$  both assumed to be 1,  $Q$  is the activation energy,  $V$  is the activation volume, and  $R$  is the molar gas constant ( $8.314 \text{ J Kmol}^{-1}$ ). We then estimate the lithospheric strength by integrating the yield stress envelopes. Modeling parameters<sup>46-48</sup> are listed in Supplementary Table 1. The values assumed for the modeling parameters, such as the strain rate, affect the absolute lithospheric strength; the point remains to emphasize the strength reduction with increasing surface heat flows.

### Surface uplift modeling

The discrepancy of the topographic anomaly is modeled as a combined isostatic effect resulting from lower crustal dedensification due to partial

melting and thermal expansion from lithospheric mantle thinning. Underplating is not considered because previous subsurface imaging results indicate thinner crust beneath areas with higher compressional-to-shear wave velocity ratios<sup>16</sup>. Uplift  $\delta h^1$  resulting from dedensification is

$$\delta h^1 = z_l \frac{\delta \rho}{\rho_m}, \quad (10)$$

where  $z_l$  is the lower crustal thickness assumed to be 20 km,  $\rho_m$  is the mantle density, and  $\delta \rho$  is the density change computed as a function of melt and volatile fraction  $M$ :

$$\delta \rho = M(\rho_{\text{solid}} - \rho_{\text{molten}}), \quad (11)$$

and  $\rho_{\text{solid}}$  and  $\rho_{\text{molten}}$  are the densities of the solid and molten lower crust. The melt and volatile fraction in the lower crust is determined by

$$M = \frac{T - T_{\text{solidus}}}{T_{\text{liquidus}} - T_{\text{solidus}}}, \quad (12)$$

using the temperature at 25 km and the following liquidus and solidus relations

$$T_{\text{liquidus}}(K) = 1423 + 0.105 \times P, \quad (13)$$

$$T_{\text{solidus}}(K) = \begin{cases} 973 - \frac{70,400}{P+354} + \frac{77,800,000}{(P+354)^2}, & P < 1.6 \text{ GPa} \\ 935 + 0.0035 \times P + 0.0000062 \times P^2, & \text{Otherwise} \end{cases}, \quad (14)$$

common for lower crustal rocks, such as Gabbro. Thermal isostatic contribution to the uplift is determined by integrating from the surface to the lithosphere-asthenosphere boundary over the difference of the initial geotherm corresponding to the lowest surface heat flow measurement  $q_1$  and subsequent geotherms for higher surface heat flow values  $q_i$ ,

$$\delta h_i^2 = \alpha \int_0^{LAB_i} T_{q_i}(z) - T_{q_1}(z) dz, \quad (15)$$

where  $\alpha$  is the linear thermal expansion coefficient ( $2e-5 \text{ K}^{-1}$ ).

## Data availability

All the data used in the study are available on [Zenodo](#)<sup>49</sup>. Seismic waveforms analyzed in the study are also publicly available and can be obtained through the services of the EarthScope Consortium.

## Code availability

All computer programs and files necessary to reproduce the results and figures are available on [Zenodo](#)<sup>49</sup>.

Received: 20 November 2023; Accepted: 25 January 2024;

Published online: 12 February 2024

## References

- Wilson, J. T. Did the Atlantic close and then re-open? *Nature* **211**, 676–681 (1966).
- Brune, S. et al. Geodynamics of continental rift initiation and evolution. *Nature* **4**, 235–253 (2023).
- Buck, W. R. in *Rheology and deformation of the lithosphere at continental margins* (eds G. D. Karner, B. Taylor, N. W. Driscoll, & D. L. Kohlstedt) Ch. 1, 1–30 (2004).
- Fishwick, S. Surface wave tomography: imaging of the lithosphere-asthenosphere boundary beneath central and southern Africa? *Lithos* **120**, 63–73 (2010).
- Gallahue, M. M. et al. A compilation of igneous rock volumes at volcanic passive continental margins from interpreted seismic profiles. *Mar. Petrol. Geol.* **122**, 1–11 (2020).
- Manatschal, G. New models for evolution of magma-poor rifted margins based on a review of data and concepts from West Iberia and the Alps. *Int. J. Earth Sci.* **93**, 432–466 (2004).
- Koptev, A., Calais, E., Burov, E. B., Leroy, S. & Gerya, T. Dual continental rift systems generated by plume-lithosphere interaction. *Nat. Geosci.* **8**, 388–392 (2015).
- O'Donnell, J. P., Adams, A., Nyblade, A. A., Mulibo, G. D. & Tugume, F. The uppermost mantle shear wave velocity structure of eastern Africa from Rayleigh wave tomography: constraints on rift evolution. *Geophys. J. Int.* **194**, 961–978 (2013).
- Morley, C. K., Wescott, W. A., Harper, R. M. & Cunningham, S. M. in *Geoscience of Rift Systems—Evolution of East Africa: AAPG Studies in Geology* 44 (ed C. K. Morley) Ch. 5, 91–100 (1999).
- Morley, C. K. in *Geoscience of Rift Systems—Evolution of East Africa: AAPG Studies in Geology* 44 (ed C. K. Morley) 151–160 (1999).
- Ambraseys, N. N. The Rukwa earthquake of 13 December 1910 in East Africa. *Terra Nova* **3**, 202–211 (1991).
- Wright, L. J., Muirhead, J. D. & Scholz, C. A. Spatiotemporal variations in upper crustal extension across the different basement terranes of the lake Tanganyika Rift, East Africa. *Tectonics* **39**, 1–24 (2020).
- Roberts, E. M. et al. Sedimentology and depositional environments of the Red Sandstone Group, Rukwa Rift Basin, southwestern Tanzania: New insight into Cretaceous and Paleogene terrestrial ecosystems and tectonics in sub-equatorial Africa. *J. Afr. Earth Sci.* **57**, 179–212 (2010).
- Hilbert-wolf, H. L., Roberts, E. M. & Simpson, E. L. New sedimentary structures in seismites from SW Tanzania: evaluating gas- vs. water-escape mechanisms of soft-sediment deformation. *Sediment. Geol.* **344**, 253–262 (2016).
- Chakrabarti, R., Basu, A. R., Santo, A. P., Tedesco, D. & Vaselli, O. Isotopic and geochemical evidence for a heterogeneous mantle plume origin of the Virunga volcanics, Western rift, East African Rift system. *Chem. Geol.* **259**, 273–289 (2009).
- Hodgson, I. et al. Crustal structure at a Young Continental Rift: a receiver function study from the Tanganyika Rift. *Tectonics* **36**, 1–17 (2017).
- Hammond, J. O. S. et al. The nature of the crust beneath the Afar triple junction: evidence from receiver functions. *Geochem. Geophys. Geosyst.* **12**, 1–24 (2011).
- Tepp, G. et al. Seismic anisotropy of the upper mantle below the Western Rift, East Africa. *J. Geophys. Res.* **123**, 5644–5660 (2018).
- Jones, D. J. R. A summary of the East Africa Rift Temperature and Heat flow Model (EARTH). *Br. Geol. Surv. Open Rep. OR/20/006*, 1–24 (2020).
- Lavayssière, A. et al. Depth extent and kinematics of faulting in the Southern Tanganyika Rift, Africa. *Tectonics* **38**, 842–862 (2019).
- Hess, H. H. Seismic anisotropy of the uppermost mantle under oceans. *Nature* **203**, 629–631 (1964).
- Nicolas, A. & Christensen, N. I. in *Composition, Structure and Dynamics of the Lithosphere-Asthenosphere System* 16 (eds K. Fuchs & C. Froidevaux) 111–123 (1987).
- Fouch, M. J. & Rondenay, S. Seismic anisotropy beneath stable continental interiors. *Phys. Earth Planet. Inter.* **158**, 292–320 (2006).
- Keir, D., Kendall, J. M., Ebinger, C. J. & Stuart, G. W. Variations in late syn-rift melt alignment inferred from shear-wave splitting in crustal earthquakes beneath the Ethiopian rift. *Geophys. Res. Lett.* **32**, 1–4 (2005).
- Muirhead, J. D., Wright, L. J. & Scholz, C. A. Rift evolution in regions of low magma input in East Africa. *Earth Planet. Sci. Lett.* **506**, 332–346 (2019).
- Morley, C. K. Interaction of deep and shallow processes in the evolution of the Kenya rift. *Tectonophysics* **236**, 81–91 (1994).

27. Muluneh, A. A. et al. Mechanism for deep crustal seismicity: insight from modeling of deformation processes at the main Ethiopian rift. *Geochem. Geophys. Geosyst.* **21**, 1–13 (2020).
28. Kolawole, F., Philips, T. B., Atekwana, E. A. & Jackson, C. A. L. Structural inheritance controls strain distribution during early continental rifting, Rukwa Rift. *Front. Earth Sci.* **9**, 1–14 (2021).
29. Mulaya, E., Gluyas, J., McCaffrey, K., Phillips, T. & Ballentine, C. Structural geometry and evolution of the Rukwa Rift Basin, Tanzania: implications for helium potential. *Basin Res.* **34**, 938–960 (2022).
30. Lithgow-Bertelloni, C. & Silver, P. G. Dynamic topography, plate driving forces and the African superswell. *Nature* **395**, 269–271 (1998).
31. Perez-Gussinye, M. et al. Effective elastic thickness of Africa and its relationship to other proxies for lithospheric structure and surface tectonics. *Earth Planet. Sci. Lett.* **287**, 152–167 (2009).
32. Levandowski, W., Jones, C. H., Butcher, L. A. & Mahan, K. H. Lithospheric density models reveal evidence for Cenozoic uplift of the Colorado Plateau and Great Plains by lower-crustal hydration. *Geosphere* **14**, 1150–1164 (2018).
33. Hopper, E. et al. Preferential localized thinning of lithospheric mantle in the melt-poor Malawi Rift. *Nat. Geosci.* **13**, 584–589 (2020).
34. Njinju, E. A. et al. Lithospheric structure of the Malawi Rift: implications for magma-poor rifting processes. *Tectonics* **38**, 1–19 (2019).
35. Gerya, T. *Introduction to Numerical Geodynamic Modelling*. (Cambridge University Press, 2019).
36. van Herwaarden, D. et al. Full-waveform tomography of the African plate using dynamic mini-batches. *J. Geophys. Res.* **126**, 1–22 (2023).
37. Tian, X. & Buck, W. R. Intrusions induce global warming before continental flood basalt volcanism. *Nat. Geosci.* **15**, 417–422 (2022).
38. Pérez-Gussinye, M., Ranero, C. R. & Reston, T. J. Mechanisms of extension at nonvolcanic margins: evidence from the Galicia interior basin, West of Iberia. *J. Geophys. Res.* **108**, 1–19 (2003).
39. Savage, M. K., Wessel, A., Teanby, N. A. & Hurst, A. W. Automatic measurement of shear wave splitting and applications to time varying anisotropy at Mount Ruapehu volcano, New Zealand. *J. Geophys. Res.* **115**, 1–17 (2010).
40. Vidale, J. E. Finite-difference calculation of traveltimes in three dimensions. *Geophysics* **55**, 521–526 (1990).
41. Booth, D. C. & Crampin, S. Shear-wave polarizations on a curved wavefront at an isotropic free surface. *Geophys. J. R. Astr. Soc.* **83**, 31–35 (1985).
42. Thomas, C. & Kendall, J. M. The lowermost mantle beneath northern Asia-II. Evidence for lower-mantle anisotropy. *Geophys. J. Int.* **151**, 296–308 (2002).
43. Chapman, D. S. Thermal gradients in the continental crust. *Geol. Soc. Spec. Publ.* **24**, 63–70 (1986).
44. Turcotte, D. & Schubert, G. *Geodynamics*. (Cambridge University Press, 2014).
45. Stamps, D. S., Flesch, L. M. & Calais, E. Lithospheric buoyancy forces in Africa from a thin sheet approach. *Int. J. Earth Sci.* **99**, 1525–1533 (2010).
46. Rutter, E. H. & Brodie, K. H. Experimental grain size-sensitive flow of hot-pressed Brazilian quartz aggregates. *J. Struct. Geol.* **26**, 2011–2023 (2004).
47. Rybacki, E. & Dresen, G. Dislocation and diffusion creep of synthetic anorthite aggregates. *J. Geophys. Res.* **105**, 26017–26036 (2000).
48. Hirth, G. & Kohlstedt, D. L. in *Inside the subduction factory American Geophysical Union Monograph* (ed J. Eiler) 83–105 (2003).
49. Ajala, R. & Kolawole, F. Reproducibility material on the role of blind magmatism in nonvolcanic continental extension. <https://doi.org/10.5281/zenodo.10095512> (2023).
50. Rajaonarison, T. A., Stamps, D. S. & Naliboff, J. B. Role of lithospheric buoyancy forces in driving deformation in East Africa from 3D geodynamic modeling. *Geophys. Res. Lett.* **48**, 1–10 (2021).

## Acknowledgements

We thank Editor Joe Aslin for carefully handling our manuscript throughout the review process and reviewers Christopher Morley and Ameha Muluneh for constructive comments that improved the quality of our paper. We thank Roger Buck, Benjamin Holtzman, and Marc Spiegelman for the fruitful discussions that helped enhance the study. This project was supported by funds from the Columbia Climate School awarded to Folarin Kolawole.

## Author contributions

R.A. and F.K. conceptualized the project. R.A. analyzed the seismic data, performed the numerical modeling, and wrote the initial draft of the paper. F.K. provided geologic lineament data and structural interpretations, contributed to figure edits, and revised the paper. W.M. revised the paper.

## Competing interests

The authors declare no competing interests.

## Additional information

**Supplementary information** The online version contains supplementary material available at <https://doi.org/10.1038/s43247-024-01244-7>.

**Correspondence** and requests for materials should be addressed to Rasheed Ajala.

**Peer review information** *Communications Earth & Environment* thanks Chris Morley and Ameha Atnafu Muluneh for their contribution to the peer review of this work. Primary Handling Editor: Joe Aslin. A peer review file is available.

**Reprints and permissions information** is available at <http://www.nature.com/reprints>

**Publisher's note** Springer Nature remains neutral with regard to jurisdictional claims in published maps and institutional affiliations.

**Open Access** This article is licensed under a Creative Commons Attribution 4.0 International License, which permits use, sharing, adaptation, distribution and reproduction in any medium or format, as long as you give appropriate credit to the original author(s) and the source, provide a link to the Creative Commons license, and indicate if changes were made. The images or other third party material in this article are included in the article's Creative Commons license, unless indicated otherwise in a credit line to the material. If material is not included in the article's Creative Commons license and your intended use is not permitted by statutory regulation or exceeds the permitted use, you will need to obtain permission directly from the copyright holder. To view a copy of this license, visit <http://creativecommons.org/licenses/by/4.0/>.

© The Author(s) 2024